Composites Part B 248 (2023) 110398

Contents lists available at ScienceDirect

Composites Part B

journal homepage: www.elsevier.com/locate/compositesb

Aligned multi-walled carbon nanotube-embodied hydrogel *via* low magnetic field: A strategy for engineering aligned injectable scaffolds

Muthusamy Saranya [a], Janne T. Koivisto [a,1], Ana C.M. Carvalho [b], Fernando Sato [c], Andrea Lassenberger [d], Lionel Porcar [d], Baleeswaraiah Muchharla [e], Saikat Talapatra [e], Birgitte H. McDonagh [f], Lauriane Janssen [a], Olli Pitkänen [a], Minna Kellomäki [g], Krisztian Kordas [a], Gabriela S. Lorite [a,*]

[a] Microelectronics Research Unit, University of Oulu, Pentti Kaiteran Katu 1, 90014, Oulu, Finland
[b] Departmento de Ciências Naturais, Universidade Federal de São João Del-Rei, Praça Dom Helvécio, 74, Fábricas, São João, Del-Rei, MG, 36301-160, Brazil
[c] Departmento de Fisica, Instituto de Ciências Exatas, Campus Universitário, Universidade Federal de Juiz de Fora, MG, 36036-900, Brazil
[d] Institut Laue-Langevin, 71 Avenue des Martyrs, 38042, Grenoble, France
[e] Department of Physics, Southern Illinois University, Carbondale, IL, 62901, USA
[f] Biotechnology and Nanomedicine, SINTEF Industry, Trondheim, Norway
[g] BioMediTech, Tampere University, Korkeakoulunkatu 3, 33720, Tampere, Finland

ARTICLE INFO

Keywords:
Carbon nanotubes
Hydrogels
Magnetic field
Alignment
Injectable scaffolds

ABSTRACT

Injectable scaffolds are a promising strategy to restore and regenerate damaged and diseased tissues. They require minimally invasive procedure and allow the formation of an *in-situ* structure of any shape. However, the formation of 3D *in-situ* structure with aligned morphologies using a method which could be easily transferred to clinical settings remains a challenge. Herein, the rational design of an aligned injectable hydrogel-based scaffold *via* remote-induced alignment is reported. Carboxylated multi-walled carbon nanotubes (cMWCNT) are aligned into hydrogel *via* low magnetic field. The uniform dispersion and alignment of cMWCNT into the hydrogel are clearly demonstrated by small angle neutron scattering. The obtained aligned cMWCNT-embodied hydrogel is stable over 7 days at room temperature and as well at body temperature (i.e. 37 °C). As unique approach, the formation of MWCNT-hydrogel composite is investigated combining rheology with molecular dynamic and quantum mechanical calculations. The increase of MWCNT concentration into the hydrogel decreases the total energy promoting structural stabilization and increase of stiffness. The remote aligning of injectable hydrogel-based scaffold opens up horizons in the engineering of functional tissues which requires specific cell orientation.

1. Introduction

Design of modular and tunable injectable scaffolds is of particular interest for the repair and regeneration of damaged and diseased tissues [1]. From clinical perspective, injectable scaffolds would enable minimally invasive procedures, the formation of an *in-situ* 3D structure in the shape of the patient injury and the seeding of patient own cells. While remarkable advancements in stem cell and induced-pluripotent stem cell methodologies offer new prospects of personalized tissue replacements [2,3], a three-dimensional (3D) biomimetic scaffold is required to support the transition from cells to a functional tissue. As a rule of thumb, scaffolds should be designed to mimic the native extracellular matrix (ECM). Several natural and synthetic polymers such as chitosan, alginate and poly(ethylene glycol) have been reported to be used as injectable scaffolds [1]. Generally, these polymers are biocompatible, biodegradable and easy to modify with cell adhesive ligands and/or growth factors to modulate biological function of cells. However, they fail to provide the topological, mechanical and electrical cues necessary to promote

* Corresponding author.
E-mail addresses: muthusamy.saranya@oulu.fi (M. Saranya), janne.koivisto@ki.se (J.T. Koivisto), anaclaudia@ufsj.edu.br (A.C.M. Carvalho), fsato01@gmail.com (F. Sato), lassenberger.andrea@gmail.com (A. Lassenberger), porcar@ill.fr (L. Porcar), baleeswaraiahmuchharla@gmail.com (B. Muchharla), saikat@siu.edu (S. Talapatra), birgitte.mcdonagh@sintef.no (B.H. McDonagh), lorite.oulu@gmail.com (L. Janssen), olli.pitkanen@oulu.fi (O. Pitkänen), minna.kellomaki@tuni.fi (M. Kellomäki), krisztian.kordas@oulu.fi (K. Kordas), gabriela.lorite@oulu.fi (G.S. Lorite).
[1] Present address - Department of Laboratory Medicine, Karolinska Institutet, Alfred Nobels Allé 8, 14,152.

https://doi.org/10.1016/j.compositesb.2022.110398
Received 16 February 2022; Received in revised form 23 September 2022; Accepted 2 November 2022
Available online 5 November 2022

tissue formation.

The encapsulation of nanomaterials into polymeric matrices have been an attractive approach to improve the scaffolds properties, enabling the control of physical cues to regulate cell fate and promote tissue regeneration [4,5]. For instance, carbon nanotube (CNTs) have been used to create conductive scaffolds for applications such as neural [6–10], cardiac [11–15] tissues and muscle tissues [16] in which electrical signal propagation is crucial for functional tissue formation. Generally, the reported studies have shown that CNTs composite scaffolds are able to promote cell attachment, growth, differentiation and support long-term survival of cells [17]. CNTs have also demonstrated to sustain and promote neuronal activity in network cultured cells [18–20].

One of the major challenges of injectable scaffolds is to create a 3D structure with aligned and elongated morphologies. To create an injectable scaffold capable of inducing unidirectional cell orientation would be of relevance in several sub-fields of tissue engineering such as neural, cardiac and cartilage [21]. We have previously demonstrated that vertically aligned CNT micropillar templates is capable to induce specific guidance of human neurites and as well as seamless neuronal networks in any arbitrary shape and size [22]. Alignment of CNTs on rigid matrices have been achieved via different methods and found their applications on energy storage, sensors, thin film transistors, 3D printing and other electronic applications [23–25]. Aligned hydrogels scaffolds have been demonstrated by aligning the polymer used as main gel component (i.e. collagen and fibrin) *via* mechanical strain [26–28] and magnetic field [29–31], although the clinical application of the former method as injectable scaffold seems to be limited. Alignment of CNTs in hydrogel matrices has also been demonstrated by using dielectrophoresis [13,32,33], a non-uniform electrical field between planar metal electrodes. Overall, the reported *in vitro* studies have shown that hydrogels contained aligned CNTs are more effective to support cell differentiation and functionality than pristine or contained randomly CNT distributed hydrogels. While the reported studies are relevant for diagnostic and therapeutic tools (e.g. drug screening), the use of dielectrophoresis as driven force to align the CNTs limits its translation of the technology to *in-vivo*. Furthermore, most of the published studies on CNTs-hydrogel composites employ saturable CNTs concentration, which often causes non-uniform CNTs dispersion and aggregation thus limiting clinical applications [34].

To address these issues, we developed a new approach to uniformly integrate and align multi-walled CNTs (MWCNT) into a hydrogel matrix *via* low magnetic field (<1000 mT). Magnetic field (<3000 mT) are generally regarded safe and have been widely used in radiology (e.g. magnetic resonance imaging) [35] and drug delivery studies [36,37]. Furthermore, the Food and Drug Administration (FDA) has established that patients exposed to static magnetic field ≤8000 mT for infants (above 1 month), children and adult does not present significant risk [38]. To enhance the MWCNT response to magnetic field, MWCNT were synthesized using a precursor of xylene and ferrocene mixture. Due to the high hydrophobicity nature of the MWCNT, functionalization with carboxylate groups was performed via acid treatment, promoting easy dispersion in aqueous based solutions. This allows application in various field as well as avoid contamination and side effects arising from non-volatile solvents and additives [39]. Homogenous MWCNT water-based dispersion was obtained after MWCNT carboxylation and several centrifugation steps. The ferromagnetic behaviour of pristine MWCNT and carboxylated MWCNT (cMWCNT) was assessed. Free-standing cMWCNT-embodied hydrogels were produced with different cMWCNT concentrations. As a hydrogel model system, gellan gum (GG) which is a well-known natural polysaccharide and FDA-approved food additive was selected due its recognized properties to form hydrogels with adequate mechanical properties, high biocompatibility, no cytotoxicity and easy processability [29,40–42]. In addition, GG has been demonstrated as potential injectable vehicle for therapeutic delivery and under thermal conditions suitable for tissue engineering applications [41,42]. GG Spermine (SPM), a multivalent bioamine, was selected to cross-link the GG for a rapid and efficient gelation [43]. The alignment of cMWCNT in the GG matrix *via* low magnetic field was confirmed by small angle neutron scattering (SANS) and an *in-situ* optical arrangement. SANS is non-invasive method to investigate the structure of biomaterials composed of light elements in their native state. Hydrogels are challenging to probe with methods like conventional or cryo electron microscopy (scanning and transmission) since they require the sample to be dry, leading to non-representative results for such normally hydrated systems. SANS is a bulk method which samples the whole illuminated volume and thus delivers a very high statistical relevance, especially when compared to TEM or SEM where just a very small part of your sample is observed. The stability of cMWCNT alignment in the hydrogel matrix was investigated as a function of the time (up to 7 days) and in different conditions (i.e. temperature and presence of culture media). The mechanical properties of pristine as well as cMWCNT-embodied hydrogels were assessed *via* rheological studies. To rationalize the interaction between hydrogel and CNTs at molecular level, molecular dynamic (MD) and quantum mechanical (QM) calculations were performed. In addition to offering a new approach to injectable aligned hydrogel-based scaffolds, our work provides a comprehensive assessment on the formation of MWCNT-hydrogel composite all the way from molecular to macroscale.

2. Materials and methods

2.1. Materials

Gelzan ™ CM (LOT#SLBP7450V), spermine tetrahydrochloride (SPM), sucrose (99.5%) and sterile-filtered water were purchased from Sigma Life Science, ferrocene was purchased from Fluka, Xylene was purchased from Alfa Aesar. Nitric acid (HNO_3, purity 70%) and sulphuric acid (H_2SO_4, purity 95–98%) were purchased from Sigma Aldrich. Acetone was purchased from VWR. Neurobasal medium was purchased from Thermofisher. Si/SiO_2 wafers were purchased from Si-Mat Germany.

2.2. Synthesis of MWCNT

MWCNT were synthesized by chemical vapor deposition (CVD) in a quartz tube reactor as described elsewhere [44–46]. In short, the catalyst precursor ferrocene ($Fe(C_2H_5)_2$) was dispersed in xylene ($(CH_3)_2C_6H_4$)) at a concentration of 20 g/L. Si/SiO_2 chips were loaded on alumina boats in the reactor. The furnace was sealed with inlet consisting of a feeding tube with a copper hair ball connected to syringe, temperature probe and argon gas line and the outlet was connected to vacuum and water pump. The reactor was flushed with argon (Ar) and the furnace temperature was set to 770 °C with Ar flow at atmospheric pressure. After the temperature probe reached 150 °C, the precursor was introduced at 96 mL/h till the feeding tube looks wet, then change the rate to 6 ml/h for 60 min to facilitate the synthesis of MWCNTs.

2.3. Carboxylation of MWCNT

MWCNT (50 mg) were collected from the Si/SiO_2 chips, grinded and transferred to a beaker filled with 150 mL of nitric acid and sulphuric acid blend at a ratio of 3:1. The mixture was sonicated for 5 h in room temperature (RT). Then, the dense dispersion was repeatedly centrifuged (4000 rpm for 15 min) to replace the acid supernatant with deionized (DI) water. This mixture was filtered and washed on 0.2 μm cellulose nitrate membrane till the filtrate reached nearly neutral pH (approx. 5 L). The collected cMWCNT on the filter membrane were dried at 80 °C overnight at dry oven.

2.4. Homogenous aqueous dispersion of cMWCNT

1 mg/mL concentration was prepared in sterile water and sonicated for 30 min. Then, the dispersion was centrifuged at 4000 rpm for 15 min from which the supernatant was collected. This step was repeated until no precipitation is visually observed. The concentration was determined by weighting PVDF filter paper with dispersed cMWCNT of known volume.

2.5. Characterization of cMWCNT

The morphology and elemental chemical composition of cMWCNT were investigated by transmission electron microscopy (TEM) and energy dispersive x-ray spectroscopy (EDS). For this, few drops of cMWCNT dispersed in water were suspended in equal drops of ethanol. A drop of this suspension was dried at room temperature on copper mesh covered with Holey Carbon Film (HC300-Cu, Electron Microscopy Science). Images and elemental composition mapping were acquired on JEOL JUM 2200FS TEM. The outer diameter of 347 individual cMWCNTs were extracted using EM software Beta 0.85 (Teitz Video and Image Processing Systems GmbH). Data were then represented as column graph using OriginPro2020b. Lorentz fit was used to estimate the diameter mean of cMWCNT and result given as $d\pm\sigma$, where d is the center and σ is the standard deviation calculated as width/2. Raman spectroscopy was conducted using a Horiba Jobin-Yvon LabRAM HR800 UV–vis μ-Raman at $\lambda = 488$ nm. In this case, the cMWCNT dispersion was drop casted on a cover slip and dried overnight. Inductively coupled plasma mass spectrometry (ICP-MS) was used to quantify the amount of iron (Fe) in cMWCNT dispersions at concentrations of 0.1 and 0.025 mg/mL. MWCNT dispersions were diluted in 5% HNO3 and analysed on an Agilent 8800 Triple Quadropole ICP-MS (ICP-QQQ) with a SPS 4 Autosampler. The samples have been quantified against standards from Inorganic Ventures. The results are given with concentrations in mg/L and relative standard deviations (RSD) in %. Three measurements were performed for each sample. The reported values are on the same sample and the RSD is the instrument deviation for the ICP-MS. The magnetic properties of pristine MWCNTs and cMWCNT samples were measured using a Quantum Design's VersaLab system installed with Vibrating Sample Magnetometer (VSM) option which can operate in a wide range of temperature from 50 K to 400 K and magnetic field can be applied up to 3 T.

2.6. Preparation of pristine gellan gum (GG) and cMWCNT-embodied GG

Pristine GG solution was prepared at 10% (w/w) sucrose solution at 5 mg/mL. The GG was dissolved by heating at 90 °C in water bath in short interval till the solution became clear and filtered using Sterivex™ 0.2 μm filter (Merck Millipore). 0.02 mg/mL cMWCNT in 5 mg/mL GG was prepared by mixing equal amount of 10 mg/mL GG solution and 0.04 mg/mL cMWCNT diluted in 10% (w/w) sucrose at 90 °C. Similarly, 0.1 mg/mL cMWCNT in GG was prepared by using 0.2 mg/mL cMWCNT in 10 mg/mL GG. Crosslinker SPM was prepared at 0.35 mg/mL concentration in 10% sucrose [29]. For hydrogel preparation, the solutions were placed in water bath at 37 °C. SPM and GG or cMWCNT embodied GG were mixed at a ratio of 1:6.25 under constant stirring and casted into a suitable mould (*e.g.* cuvette or syringe) [29,47].

2.7. Preparation of aligned cMWCNT-embodied GG

To investigate the alignment of cMWCNT into GG matrix, the pristine GG and cMWCNT-embodied GG hydrogels were prepared as described above and immediately placed in the bore of an electromagnet for 10 min. The applied magnetic field was either 600 or 1000 mT and monitored by a magnetometer. Control samples were prepared without applying an electromagnet (i.e., at 0 mT).

2.8. Small-angle neutron scattering (SANS)

The alignment of the MWCNT in the GG matrix was investigated using SANS. SANS experiments were performed on the instrument D22 at the Institute Laue-Langevin in Grenoble, France. The neutron wavelength was set to 6.0 Å and the sample-to-detector distance set to 17.6 and 5.6 m to cover a q-range of $0.0025\ \text{Å}^{-1} < q < 0.4\ \text{Å}^{-1}$ with q being the scattering vector $q = 4\pi/\lambda \sin\vartheta$, and 2ϑ the scattering angle between the incident and the scattered neutron beam. Acquisition time was set to 30 min. Boron carbide (B4C) was used as neutron absorber, measurement temperature was set to 25 °C, 2D data was corrected for the electronic background and the empty cell and normalized to absolute scale using the transmission of the empty beam. Data were azimuthally averaged to yield the typical 1D intensity distribution I(q). For analysis of the anisotropy, I(q) was averaged for q-values of 0.0048–0.0072 Å^{-1} and plotted against the azimuthal angle. Samples were prepared in 30% D_2O and 70% H_2O solvent which correspond to the neutron scattering length density of the gellan gum ($1.51 \times 10^{-6}\ \text{Å}^{-2}$) (contrast matching the gellan gum) and allowing to study the structure and alignment of the CNTs within the gum. Data were reduced with the grasp software [48] provided at the beamline. Raw and reduced data are available at doi: http://doi.ill.fr/10.5291/ILL-DATA.9-11-1960 [49]. 1D data were fitted using IgorPro with NCNR SANS reduction macros and SASview [50].

2.9. In-situ optical arrangement

An *in-situ* optical arrangement was used for measuring the optical transmission through the hydrogels at various optical polarization angles in reference to the magnetic field direction (Fig. 3). The optical arrangement consists in a beam of a random polarized HeNe laser passing through a polarizer by which the polarization plane of $\vec{E}$ is set ($-90° < \varphi < 90°$ in reference to $\vec{B}$). The transmitted power is measured by a Laser power and Energy Meters equipped with a photodetector. Note that the transmission decreases with the increase of MWCNT concentration. The measurements were performed 10 min after the magnetic field was applied. For stability measurements, the transmission versus the polarization angles were measured at day 0, 1, 3 and 7. A minimum of 3 samples were prepared independently and measured using the *in-situ* optical arrangement for each studied condition. Results are reported as representative graphs of all the performed measurements.

2.10. Rheology

The mechanical properties cMWCNT-embodied GG were analysed using rotational rheometer MARS40 (Thermo-Haake, Germany) with Ø 20 mm titanium parallel-plate measurement geometry and 1.5 mm gap height. Samples were prepared in cut syringe moulds, covered with parafilm, stored at room temperature overnight to allow gelation process to be complete and then measured. The measurement temperature was kept constant at 37 °C with a Peltier-plate and an accompanying temperature control element and evaporation cover. First, amplitude sweep measurements were conducted to 5 parallel samples with amplitude strain range 0.0001–10.0% and constant 1 Hz frequency. This way we determined the strain amplitude range in which the dynamic mechanical properties of the material are independent of strain amplitude, i.e. the linear viscoelastic region (LVER). Next, frequency sweep with range 0.1–10 Hz, was used to verify the gel-like material behaviour of the cMWCNT-embodied GG. The strain amplitude was kept constant during a frequency sweep at a material-dependent value ($\gamma = 0.02$ for pristine GG, $\gamma = 0.005$ for cMWCNT-embodied GG at MWCNT concentration of 0.1 mg/mL, and $\gamma = 0.01$ for cMWCNT-embodied GG at MWCNT concentration of 0.02 mg/mL).

2.11. Molecular dynamic and quantum mechanical calculations

Molecular Dynamic (MD) calculations were performed using the Reactive Force Field (REAX) [51], implemented in Lammps program suite [52], where temperature effects (T = 337 K) could be considered. In all these MD calculations the initial conformations were optimized to obtain the most energetically stable conformer, independently of system size. Quantum Mechanical (QM) calculations were carried out based on Hartree-Fock theory using the PM7 semi-empirical method [53] and the MOZYME routine [54] implemented at MOPAC program [55]. In the case of QM method, the geometries of the systems were not optimized due the high number of atoms.

3. Result and discussion

3.1. cMWCNT synthesis and characterization

MWCNT were synthesized by chemical vapor deposition (CVD) on Si/SiO_2 substrates in a tube reactor at 770 °C using a precursor of xylene and ferrocene mixture. During the synthesis process iron (Fe) nanoparticles are co-deposited inside the hollow nanotube, enhancing the MWCNT response to external magnetic field. Vertically aligned MWCNT with height ranges from 400 μm to 600 μm were obtained and detached from the templates by simply scratching the SiO_2 surface with spatula. The obtained pristine MWCNT were then carboxylated. The introduction of carboxyl functional groups and as well the presence of Fe nanoparticles were confirmed by energy dispersive x-ray spectroscopy (EDS) (Fig. 1A). In addition, the mass of Fe in cMWCNT dispersions were quantified by ICP-MS (Table 1), showing that the Fe content corresponds to 0.8% of the total mass of cMWCNT. The outer diameter distribution was obtained from TEM images indicating that the diameter of cMWCNT is found to be 30 ± 9 nm (Fig. 1B–C). The typical D and G bands of sp^3 and sp^2 hybridized carbon for MWCNTs was observed by the means of Raman spectroscopy measurements (Fig. 1D). The ratio of intensity of D/G peaks (I_D/I_G) was found to be 0.85 for carboxylated MWCNT (cMWCNT), while earlier work has found 0.46 for pristine MWCNT [56].

Table 1
Concentration of iron obtained by ICP-MS for each cMWCNT concentration, and corresponding mass percentage of iron from total mass of cMWCNT dispersion.

Concentration of cMWCNT dispersion (mg/mL)	Measured concentration of iron (mg/mL) by ICP-MS	RSD (%)	Mass percentage of iron from total mass of MWCNT dispersion (%)
0,100	0,00081	1,0	0,80
0,025	0,00020	2,6	0,79

The increase of ratio of intensity from pristine to cMWCNT indicated the amount of defect created during 5 h of carboxylation.

The ferromagnetic behaviour of both pristine MWCNT and cMWCNT was confirmed by the magnetic field dependence of magnetization (M – H curves) taken at temperatures 400 K and 50 K (Fig. 1E and F). It can be observed that both pristine MWCNT and cMWCNT display hysteresis indicating the presence of ferromagnetism. In general, MWCNT show no magnetic ordering, however, the presence of metal catalysts remained in the nanotubes after the growth results in ferromagnetic behaviour [39,57]. For both samples at high temperature (i.e. 400 K), hysteresis loops are constricted, indicating the presence of more than one ferromagnetic phase, which with the decrease in temperature results in a single dominated ferromagnetic phase. M – H hysteresis loops were repeated at various temperatures to obtain the saturation magnetization versus temperature for both samples (Fig. 1G, respectively). Temperature dependence of saturation magnetization of a ferromagnetic material will be governed by Bloch's law given by Equation (I),

$$M_S(T) = M_S(0)\left[1 - \left(\frac{T}{T_C}\right)^{\alpha}\right] \quad \text{(I)}$$

where M_S (0) is spontaneous magnetization at absolute zero and T_C is Curie temperature. Generally, the exponent $\alpha = 1.5$ for bulk materials and $\alpha > 2$ for ferromagnetic nanoparticles [58,59]. The obtained data fits well with Bloch's law giving $M_S(0) = 4.9$ emu/g and 2.4 emu/g, exponent $\alpha = 2.4$ and 2.2 and $T_C = 650$ K and 684 K for pristine MWCNT

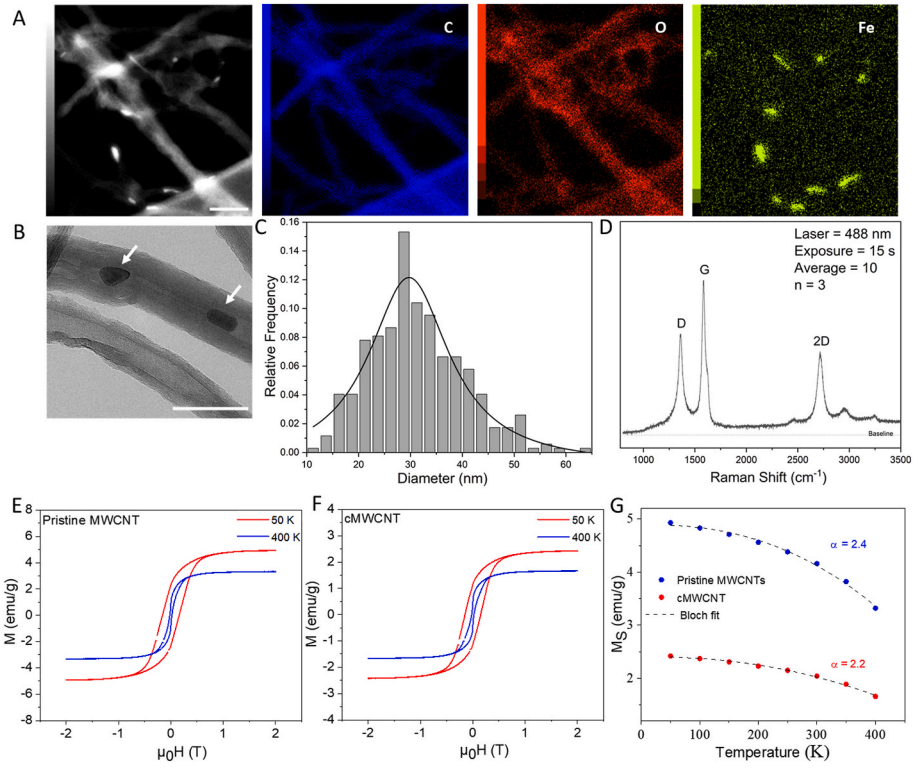

Fig. 1. Physicochemical characterization of cMWCNT. (A) EDS mapping: Carbon (marked as C), oxygen (marked as O) and iron (marked as Fe) (Scale bar 50 nm). (B) TEM images of cMWCNT, white arrow: Fe nanoparticles encapsulated in the cMWCNT (Scale bar 50 nm). (C) Diameter distribution for cMWCNT measured from series of TEM images. (D) Raman spectrum of cMWCNT. (E-F) Magnetic field dependence of magnetization plotted at 50 K and 400 K for (E) pristine MWCNTs and (F) cMWCNT. Saturation magnetization (G) versus temperature for pristine MWCNT and cMWCNT.

and cMWCNT, respectively. Therefore, the ferromagnetic ordering present in these samples resemble ferromagnetic nature of nanoparticles which could be plausible mechanism due to metal catalysts present in the nanotubes. At 50 K the values of saturation magnetization (M_S) of pristine MWCNTs and cMWCNT are determined to be ~4.93 emu/g and ~2.42 emu/g, respectively. Saturation magnetization decreased to ~3.32 emu/g for pristine MWCNTs and ~1.66 emu/g for cMWCNT with increase in temperature to 400 K. The obtained data clearly indicating that carboxylation of MWCNTs decreased the magnetization compared to pristine MWCNT. The reduced magnetization of the cMWCNT can be justified by the partial dissolution of the catalyst nanoparticles (i.e. iron) during the carboxylation process. Yet, it is clear that a residual iron remains encapsulated inside of the cMWCNT yielding a considerable ferromagnetic polarization, which can be used to induce spatial alignment of nanotubes in aqueous dispersions by an applied magnetic field [39].

3.2. Design of aligned cMWCNT-embodied GG

The cMWCNT-embodied hydrogel was produced by mixing a homogenous cMWCNT aqueous dispersion into the GG solution, which was then cross-linked by SPM. The concentrations and ratios of GG and SPM were selected based on previous work [29] to achieve gelation in few minutes. The cMWCNT-embodied GG were obtained as freestanding scaffolds having different cMWCNT concentrations (Fig. 2A). Homogenous dispersion of cMWCNT in aqueous solution prior to mixing with GG is crucial to produce cMWCNT-embodied GG without cMWCNT agglomerates or clamps, and to enable isotropic alignment of the cMWCNT inside of the formed hydrogel. The homogeneous dispersion of cMWCNT in aqueous solution is achieved up to 0.25 mg/mL by adopting a protocol originally developed to produce water based MWCNT inks for printed electronics [30].

The alignment of the cMWCNT into the GG matrix was performed by placing cuvettes filled with pristine GG/SPM or cMWCNT/GG/SPM in the bore of an electromagnet. Based on the knowledge that cMWCNTs achieve full alignment in water-based solution within few seconds [39] and GG is crosslinked in 2–5 min after adding SPM [29], a 10min exposure time to the magnetic field was selected to ensure that the cMWCNT-embodied GG is fully gelated before moving the hydrogel to the experimental conditions. A magnetic field of 1000 mT was applied on cMWCNT/GG mixture at a cMWCNT final concentration of 0.1 mg/mL. The alignment of the cMWCNT-embodied GG was confirmed *via* small-angle neutron scattering (SANS) as shown in Fig. 2B–E). All measurements were taken at the contrast match point of GG (30% D_2O), i.e. the GG contrast is matched to D_2O and the signal stems from cMWCNT only. The 1D scattering patterns of cMWCNT dispersed in a solution of 30% D_2O (grey triangle), cMWCNT-embodied GG at 0 mT (black squares) and cMWCNT embodied GG at 1000 mT (red circles) were azimuthally averaged to yield the typical 1D intensity distribution I (q) (Fig. 2 B). In all three samples, there was no sign of aggregation within the cMWCNT and a I(q) dependency of q^{-1} around q = 0.007 $\AA^{-1}$ was observed, which is typical for elongated objects. All data were fitted with a cylinder model, yielding a cMWCNT radius of 15.1 ± 0.05 nm (cMWCNT 0 mT), 15.1 ± 0.08 nm (cMWCNT embodied GG 0 mT) and 15.1 ± 0.14 nm (cMWCNT embodied GG_1000 mT), which is in good agreement with our TEM measurements, showing that the structure of cMWCNT is not altered upon incorporation into the GG. The 2D scattering pattern of cMWCNT embodied GG at 0 mT (Fig. 2C) and cMWCNT embodied GG at 1000 mT (Fig. 2D) were both acquired in 30% D_2O solvent matching the structure of GG. The anisotropy pattern was clearly observed (Fig. 2D), due to the magnetic field polarization of the encapsulated iron nanoparticles in the cMWCNT. This anisotropy was further analysed by averaging the scattering intensity over a narrow q-range of 0.0048–0.0072 $\AA^{-1}$ (as indicated in Fig. 2E, inset) and plotting it against the azimuthal angle (Fig. 2E). In particular, this result highlights the intensity variation in dependence of the azimuthal angle for aligned cMWCNT embodied GG at 1000 mT (red dots), whereas no variation is observed for the sample prepared without applying magnetic field (i.e. cMWCNT/GG 0 mT, black dots). The major orientation plane is aligned with respect to the incoming neutron beam, which corresponds to the direction of the magnetic field.

The alignment of the cMWCNT-embodied GG was corroborated by measuring the optical transmission at various optical polarization angles with reference to the magnetic field direction (Fig. 3). In such *in-situ* optical arrangement, the maximum/maximum transmission is detected when the cMWCNT is aligned perpendicular/parallel to the polarization plane (Fig. 3B). As expected, the transmitted intensities vary according to the cMWCNT concentration, which is related to the degree of absorption in and scattering on the cMWCNT. The alignment of the cMWCNT into GG matrix was also demonstrated for lower magnetic field (i.e. 600 mT) at a cMWCNT final concentration of 0.1 mg/mL (Fig. 4A and D, black curves). However, for lower concentrations of cMWCNT (i.e. 0.02 mg/mL) higher magnetic field (i.e. 1000 mT) was required to achieve alignment (Fig. 4 B, C, E and F, black curves). Therefore, higher magnetic field is required to achieve cMWCNT alignment for lower concentrations of cMWCNT in GG. The selected 10

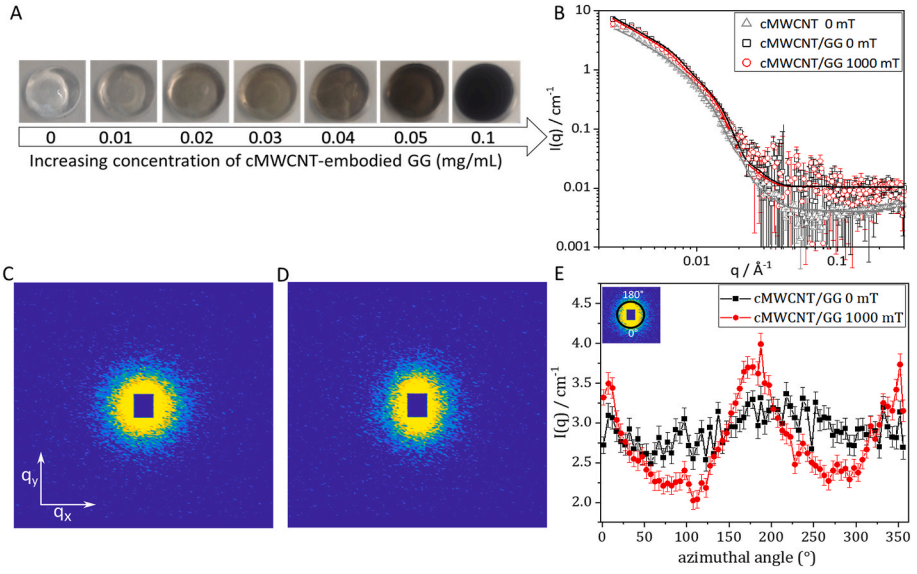

Fig. 2. A) Freestanding cMWCNT-embodied hydrogel with different concentrations of cMWCNT (B) SANS intensities for cMWCNT dispersed in a solution of 30% D_2O (grey triangle), cMWCNT-embodied GG at 0 mT (cMWCNT/GG 0 mT, black squares) and cMWCNT-embodied GG at 1000 mT (cMWCNT/GG 1000 mT, red circles). (C-D) 2D SANS patterns of cMWCNT/GG in 30% D_2O at 0 mT (C) and cMWCNT/GG in 30% D_2O at 1000 mT (D). (E) Average of the scattering intensity I(q) for q = 0.0048–0.0072 $\AA^{-1}$ (inset) of the 2D patterns in (C) and (D), plotted against the azimuthal angle. (For interpretation of the references to colour in this figure legend, the reader is referred to the Web version of this article.)

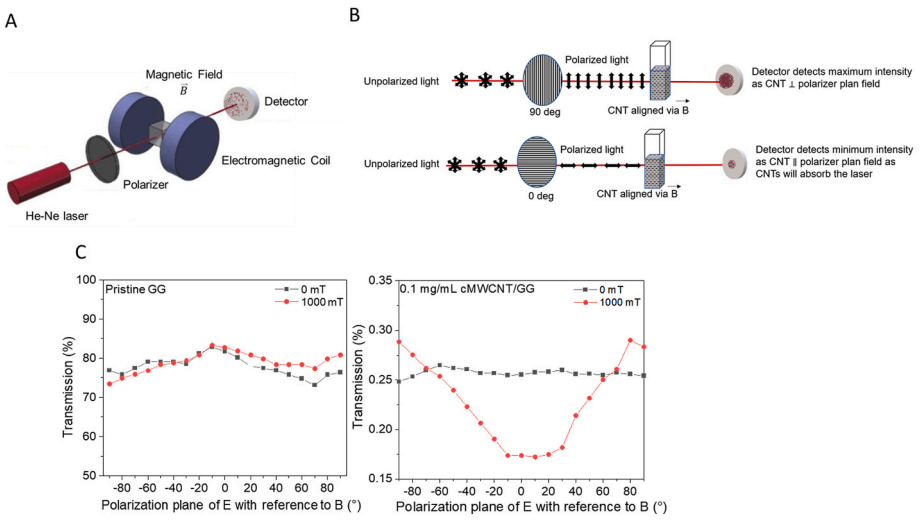

Fig. 3. A) Schematic of electromagnetic setup along with optical arrangement used for alignment and measuring of cMWCNT embodied GG, respectively. B) Schematic illustrating the two-extreme condition of laser interaction with polarizer and aligned cMWCNT-embodied GG on the detector. C) Transmission (%) with respect to the polarization plane and optical transmission for pristine GG and 0.1 mg/mL cMWCNT embodied GG at room temperature (RT) using the optical arrangement.

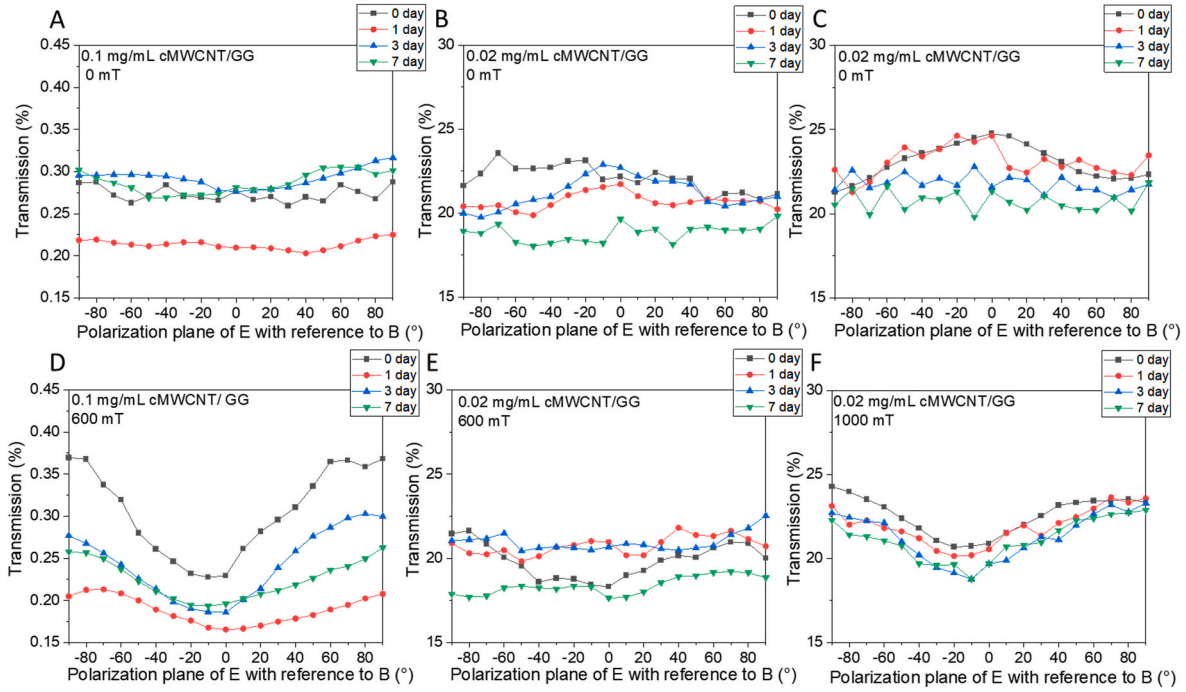

Fig. 4. Transmission (%) with respect to the polarization plane and optical transmission for 0, 1, 3 and 7 days at RT. (A) 0.1 mg/mL cMWCNT/GG at 0 mT, (B-C) 0.02 mg/mL cMWCNT/GG at 0 mT, (D) 0.1 mg/mL cMWCNT/GG at 600 mT, (E) 0.02 mg/mL cMWCNT/GG at 600 mT and (F) 0.02 mg/mL cMWCNT/GG at 1000 mT. Note that data showed in (B) is from a different sample than data showed in (C) and used as control sample regarding the data showed in (E), while (C) was taking as control sample regarding the data showed in (F). Data for pristine GG under same conditions are not shown since no alignment is observed.

min exposure time demonstrated to be enough time for cMWCNTs to achieve alignment before GG is fully crosslinked independent of cMWCNT concentration and/or magnitude of magnetic field.

3.3. Stability of cMWCNT-embodied GG regarding time, temperature and presence of culture media

To investigate the stability of the aligned cMWCNT-embodied GG, a series of measurements over time applying different conditions was performed (Fig. 4). At room temperature (RT), while the alignment of cMWCNT-embodied GG seems to weak overtime for 0.1 mg/mL aligned at 600 mT (Fig. 4D), it remains up to 7 days for 0.02 mg/mL aligned at 1000 mT (Fig. 4F). A slight shift of the minimum/maximum transmission was observed, which could be related to changes of the GG structure (e.g., dehydration). This hypothesis is based on the common knowledge that water evaporation will affect the gel structure, which is as well the reason of the controversial acceptance for the use of scanning electron microscopy (SEM) as an imaging tool for hydrogel characterization [60–62]. While there is clear evidence of the drying effects of GG at microstructure level when using different drying techniques [63], it is

still an open question how natural evaporation at RT will affect the gel microstructure along the time. A shift of the minimum/maximum transmission means that the orientation of the alignment has changed. Thus, assuming that the GG microstructure sightly changes due to water evaporation (i.e. dehydration), a slight change of the orientation of the cMWCNT alignment may occur.

By aiming to employ this system as an injectable scaffold for tissue engineering, the aligned cMWCNT-embodied GG was kept in 37 °C with and without culture media for 7 days (Fig. 5). At 37 °C without the presence of culture media, the alignment stability is comparable to the aligned cMWCNT-embodied GG stored in RT (Fig. 5A and C). In this case, the shift of the maximum/minimum transmission intensity is more evident, which is in agreement with our hypothesis that the dehydration of the GG matrix along the time takes places. The alignment is lost at day 1 after the introduction of culture media (Fig. 5B and D), which could be explained by the fact that the addition of culture media increases the GG crosslinking density and mechanical strength by forming tighter crystalline junction zone [64,65], hence changing the anisotropy achieved right after the applied magnetic field.

3.4. cMWCNT-embodied GG mechanical properties

The mechanical properties of the cMWCNT-embodied GG were investigated by rotational rheometer, which provides information on the structural properties of the hydrogel network, efficiency of polymer crosslinking, and on the interactions between the cMWCNT and gel host in the composite hydrogel [66,67]. The sweep verified that the sample shows a linear response to shear, with a slight upward trend at higher frequencies (Fig. 6A), indicating that the cMWCNT-embodied GG presents the gel-like behaviour regardless of the cMWCNT concentration or alignment. At frequencies higher than 10 Hz the system becomes unstable (data not shown). Average values of storage (G′) and loss (G″) moduli were obtained from the LVER as indicators of the hydrogel stiffness. As is typical for a self-standing gel, the obtained ratio G'/G″ for the cMWCNT-embodied GG is close to 10 [68]. The simultaneous and equal increase in G′ and G″ indicates stiffening response to higher frequency shear caused by rigidity of the crosslinked polymer network. Moreover, the increase of cMWCNT concentration slightly and gradually increases the storage moduli, suggesting good interaction between GG and cMWCNT. This result is in agreement with the previous work that hybrid CNT hydrogels albeit different technique was used to evaluate the mechanical properties [69]. In the amplitude sweep, a clear linear viscoelastic region (LVER) was observed for all hydrogels, after which the samples start to yield, and then a cross-over point is noted (Fig. 6B). At the nonlinear elastic region at the end of LVER, all tested samples have a short rise in G″ before starting to yield. The rise in G″ is a typical rheological response at larger amplitude oscillatory shear called "weak strain overshoot" and is associated with intermolecular hydrogen bonding and a weak secondary network resisting the deformation [67]. When an increased stress is applied to a viscoelastic material, the dissipation of energy *via* viscous flow occurs and is essentially measured by G''. However, as the shear amplitude and rate increase too much, dissipation increases until it cannot deal with all the energy input anymore, the polymer chains do not have enough time to relax and the peak in G″ is observed before the material yields. This is a quite common phenomenon in polysaccharide gels [67,70]. Moreover, the yield point (i.e. where G′ and G″ are equal) is gradually shifting towards higher amplitudes and higher moduli values confirming the strengthening effect caused by cMWCNT in the hydrogel. This result is also supported by the obtained average values of G′ and G″ at LVER, which clearly highlights the gradual increase of stiffness when the cMWCNT concentration increases (Fig. 6C). The alignment of the cMWCNT into the GG matrix did not affect the G′ and G″ while comparing to non-aligned cMWCNT-embodied GG (Fig. 6C). This might be explained by the direction of the cMWCNT alignment and direction of forces applied during rheological measurement. Previous work has reported that the Young' modulus for horizontally aligned CNT hydrogel was similar to non-aligned (i.e. random) CNTs hydrogel while an increase of Young's

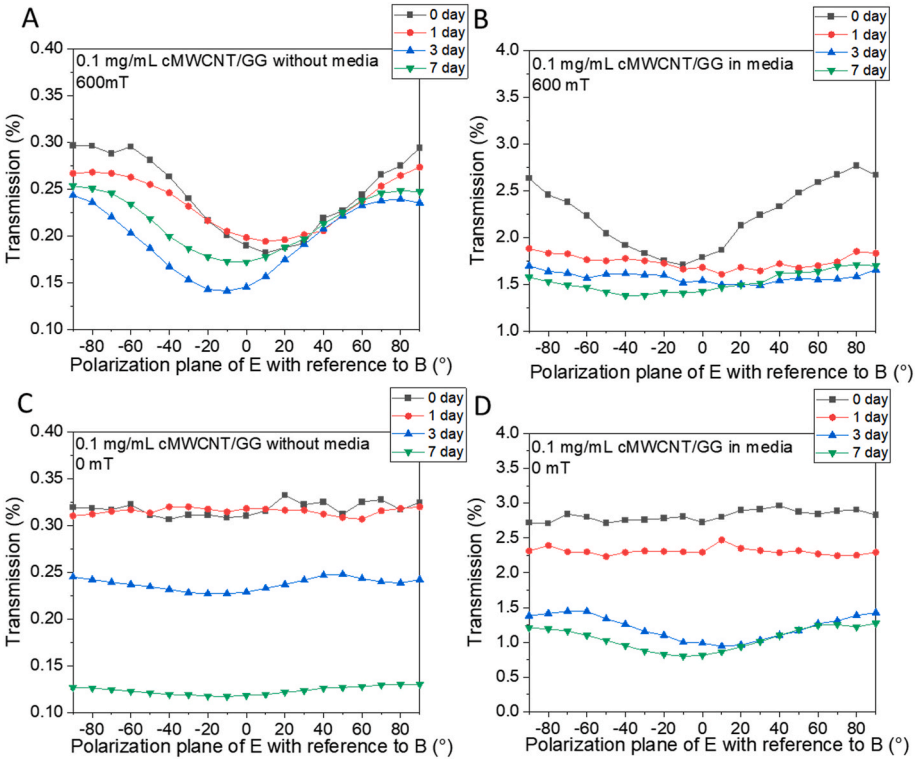

Fig. 5. Transmission (%) with respect to the polarization plane and optical transmission for 0.1 mg/mL cMWCNT- embodied GG at 37 °C for 0, 1, 3 and 7 days. (A) 600 mT, without culture media. (B) 600 mT with culture media. (C) 0 mT without culture media. (D) 0 mT with media.

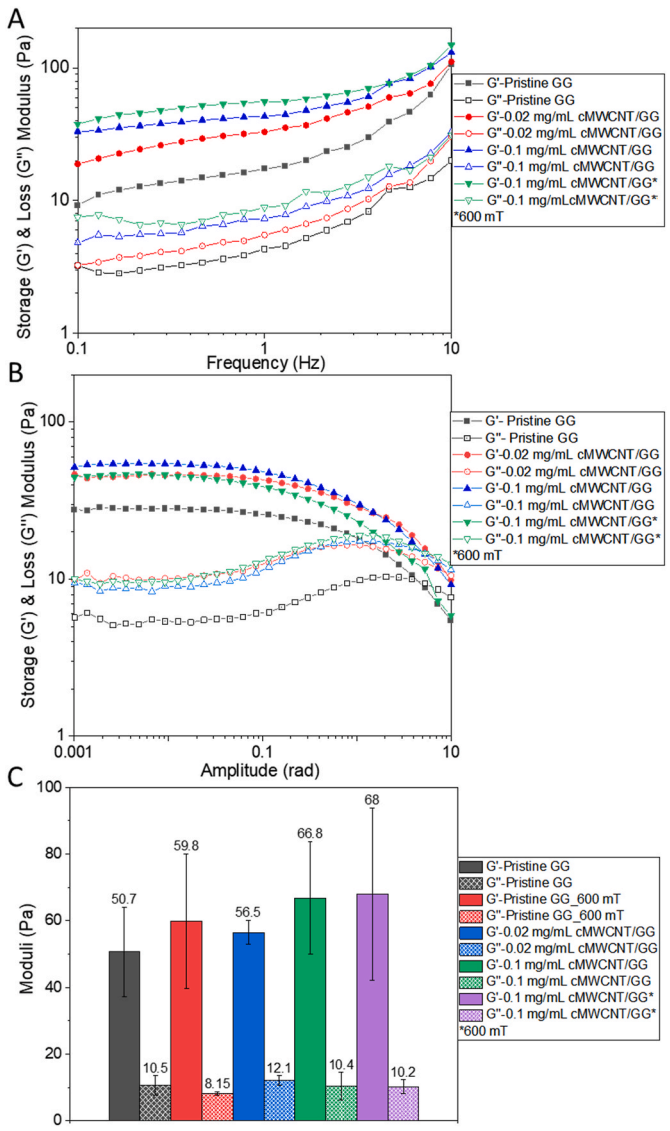

Fig. 6. Rheological testing of the pristine GG, pristine GG, 0.02 mg/mL cMWCNT/GG, 0.1 mg/mL cMWCNT/GG and aligned 0.1 mg/mL cMWCNT/GG (at 600 mT). (A) Representative curves of frequency sweep. (B) Representative curves of amplitude sweep (C) Average values of G′ and G″ at LVER (n = 3).

modulus was observed for vertically-aligned CNT hydrogel [69]. Indeed, CNTs present better mechanical properties in their axial direction than radial direction [71]. Thus, in non-aligned cMWCNT-embodied GG is expected that there are always cMWCNTs in a favourable alignment taking the load applied during rheology measurements, resulting in a clear reinforcing of the composite hydrogel. In contrast, in the aligned cMWCNT-embodied GG, the force from rotational rheometer might be coming perpendicular to the cMWCNTs and thus, the reinforcing effect is reduced but still more profound than in the pristine GG. The average values obtained for G′ and G″ also indicates that the stiffness for pristine GG can be increased by applying magnetic field during gelation.

3.5. Molecular dynamics and quantum mechanical calculations on CNT-GG interaction

Molecular dynamic (MD) and quantum mechanical (QM) calculations were carried out to rationalize the experimental findings and understand how CNTs interacts with GG+SPM matrix. For the calculations, a bundle of single-walled CNTs was used instead of MWCNT (here named as CNT). The proportion of atoms for constituent molecules on the final system (i.e. GG+SPM+CNT) was estimated based on the experimental concentrations used in this work. Note that the theoretical values for the concentrations are an estimate, since there is no straightforward correlation between concentrations used in the experimental work and the number of atoms for each individual molecule in the system. The calculations were performed considering low-to-high (<0.1 mg/mL) and super-high (>0.9 mg/mL) CNT concentrations. The energy (E) of complex formation for the studied system is given by Equation (II):

$$E_{\text{complex formation}} = E_{\text{CNT+xGG+ySPM}} - \left(E_{CNT} + E_{\text{xGG+ySPM}}\right) \quad \text{(II)}$$

where y and x correspond to the number of GG and SPM model molecules in each system. The formation energy was calculated considering the total energy calculated for each individual molecule and as well for the system MD calculations (see Supporting Information, Table S1). The obtained theoretical calculations showed that GG+SPM system has low formation energy, which increases with the CNT insertion (Fig. 7A). It is well known that in conservative systems, the force acting on a particle within a system equals the negative derivative of the energy system. Therefore, the addition of low concentrations of CNT (<0.02 mg/mL) to the GG+SPM system generates a local energetic/structural unbalance that spread throughout the entire system as a consequence of the decreasing of internal forces on CNT+GG+SPM system. Yet, this finding does not seem to reflect in the storage modulus, which was experimentally showed to slightly increase by adding 0.02 mg/mL of cMWCNT to the GG+SPM (Fig. 6C, solid black and blue). For high CNT concentrations (>0.04 mg/mL) the formation energy starts to decrease (Fig. 7A), suggesting that the increase of CNT concentration enhances the system stability. For super-high concentrations (>0.9 mg/mL), QM calculations were performed considering a CNT with chirality (40, 0), diameter around 32.32 Å and length around 101.95 Å. This model molecule has 3840 atoms, 3760 of which are carbon and 80 are hydrogen. The number of GG molecules were fixed while varying the number of CNTs inside the GG+CNT system. Note that only structures with GG and CNT molecules were considered since that in super-high concentration the presence of SPM do not generate significant effect in the total energy values. Four structures of zCNT+xGG were considered with x being 48, 96, 120 and 240. Increasing the size of GG structures around the tube means to maximize the interaction between the CNT and GG and minimize the interaction between inside and outside tubes, allowing to assess the role played by the CNT insertion on the GG matrix. Our findings verify that the increasing number of CNTs stabilizes energetically all the xGG structures independently of the number x of GG molecules (Fig. 7B–E). As expected, the internal forces increase with the inclusion of CNT into the xGG structures (Fig. 7F). Nevertheless, there is point force which is reached after certain amount of CNT is inserted in the GG system. In summary, the MD and QM calculations indicate that at low concentrations of CNT an energetic unbalance into the GG matrix; as more CNT is inserted to the matrix, the internal forces increase decreasing the total energy in the system and promoting structural stabilization of the system.

4. Conclusion

We have successfully developed a reproducible method to uniformly integrate and align cMWCNT into hydrogel matrices using low magnetic field. The cMWCNT embodied GG can be injected right after mixing the components (while it is still in liquid form) and the alignment can be achieved before the crosslinking is completed, providing a proof-of-concept that it can be used as an aligned injectable scaffold. In addition, it has been demonstrated that the injectable scaffold can be tuned to any shape as different moulds have been used according to the requirements of each used characterization techniques (e.g. thin glass vial for SANS, round syringe for rheology, UV cuvette for optical arrangement). The cMWCNT alignment into GG is best achieved at cMWCNT

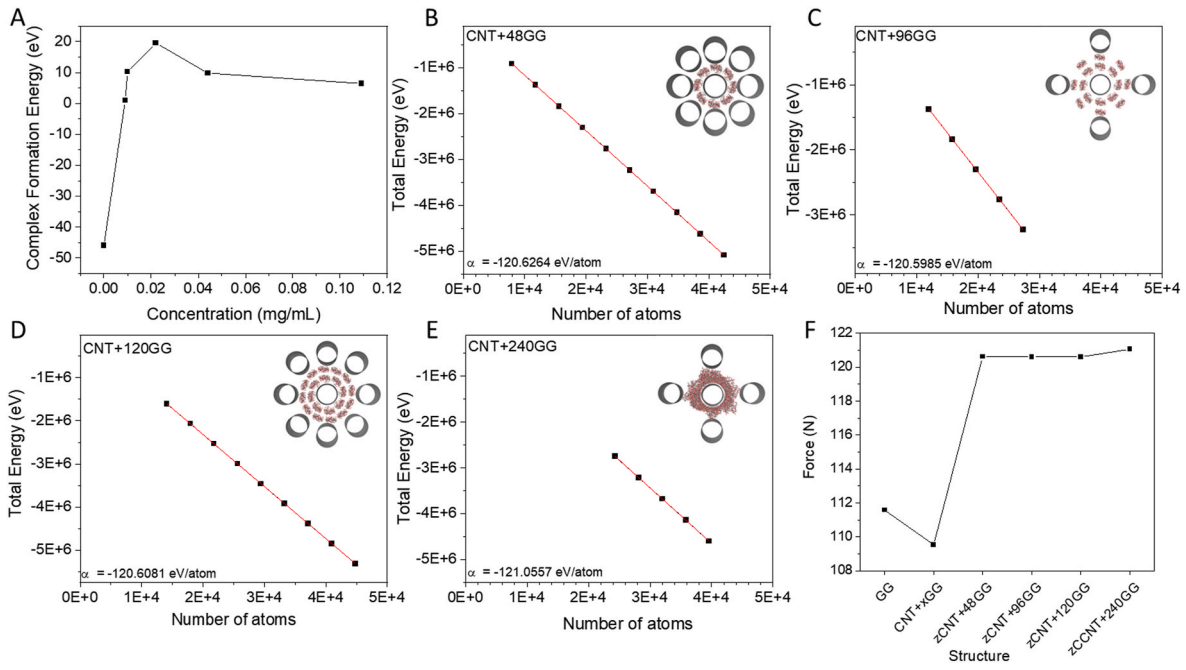

Fig. 7. MD and QM calculations. (A) Formation energy for the GG+SPM and GG+SPM+CNT for different CNT concentrations based on MD calculations. (B-E) Total energy vs number of atoms for (B) zCNT+48GG, number of nanotubes varies from 1 to 9 (insert: top view of system with nine CNTs and 48 GG molecules). (C) zCNT+96GG, number of CNTs varies from 1 to 5 (insert: top view of system with five CNTs and 96 GG molecules). (D) zCNT+120GG, number of nanotubes varies from 1 to 9 (inset: top view of system with nine carbon nanotubes and 120 GG molecules). (E) zCNT+ 240GG, number of CNTs varies from 1 to 5, (insert: top view of system with five CNTs and 240 GG molecules. (F) Calculated force for each system according to the function $F = -\nabla E$.

concentrations of 0.1 mg/mL for magnetic fields of 600–1000 mT. The alignment of cMWCNT into GG remains up to 7 days at RT and 37 °C. According to *in-situ* optical measurements, the alignment slightly changes its orientation along the days due to dehydration. No alignment was seen after day 1 with introduction of culture media in the samples, which might occur due to the formation of tighter crystalline junction zone in GG. The use of other hydrogels should be considered to overcome this challenge. SANS measurements showed the uniform dispersion of cMWCNT into the GG matrix and the anisotropy of the system after applying a magnetic field. Rheologically, the stiffening of the GG is observed with increase cMWCNT concentration, which is supported by MD and QM calculations. The proposed strategy offers a promising and feasible method to create an aligned injectable scaffold *in-situ* by applying low external magnetic fields, opening new possibilities for engineering tissues such as cardiac, neural and muscle which structural orientation and electrical cues are of fundamental importance to recover tissue function.

Author contributions

The manuscript was written through contributions of all authors. All authors have given approval to the final version of the manuscript. ‡These authors contributed equally. (match statement to author names with a symbol).

Funding sources

This work received funding from Academy of Finland (#317437 and #320090) and as well from European Union's Horizon 2020 research and innovation programme (FILL2030 project/GA #731096 and RESTORE project/GA #814558). This work benefited from the use of the SasView application, originally developed under NSF award DMR-0520547. SasView contains code developed with funding from the European Union's Horizon 2020 research and innovation programme under the SINE2020 project, grant agreement No 654000. This work received financial support from the Brazilian Research Council CNPq, CAPES, FAPEMIG, and FINEP.

Author statement

Muthusamy Saranya: conceptualization, validation, formal analysis, investigation, writing – original draft, visualization. **Janne T. Koivisto:** formal analysis, investigation, writing – contribution to original draft. **Ana C.M Carvalho:** formal analysis, investigation, writing – contribution to original draft. **Fernando Sato:** formal analysis, investigation, writing – contribution to original draft. **Andrea Lassenberger:** validation, formal analysis, investigation, resources, writing – contribution to original draft. **Lionel Porcar:** formal analysis, investigation, writing - review & editing. **Baleeswaraiah Muchharla:** formal analysis, investigation, writing – contribution to original draft. **Saikat Talapatra:** formal analysis, investigation, writing - review & editing. **Birgitte H. McDonagh:** formal analysis, investigation. **Lauriane Janssen:** conceptualization, supervision. **Olli Pitkänen:** writing - review & editing, visualization, supervision. **Minna Kellomäki:** writing - review & editing. **Krisztian Kordas:** conceptualization, writing - review & editing **and Gabriela S. Lorite:** conceptualization, resources, formal analysis, investigation, writing – original draft, supervision.

Declaration of competing interest

The authors declare that they have no known competing financial interests or personal relationships that could have appeared to influence the work reported in this paper.

Data availability

Data will be made available on request.

Acknowledgements

This paper is dedicated to the memory of our close colleague Dr. Lauriane Janssen, her kindness, endless support, and selflessness will always be remembered.

We would like to acknowledge Sami Saukko (Center of Microscopy and Nanotechnology, University of Oulu) for his assistance with TEM analyses, Senior engineer Marianne S. Kjos at SINTEF Industry for performing the ICP-MS analysis on the MWCNTs, and senior research scientist Peter P. Molesworth at SINTEF Industry for useful discussions.

Appendix A. Supplementary data

Supplementary data to this article can be found online at https://doi.org/10.1016/j.compositesb.2022.110398.

References

[1] Hou Q, Bank PA De, Shakesheff KM. Injectable scaffolds for tissue regeneration. J Mater Chem 2004;14:1915–23. https://doi.org/10.1039/B401791A.
[2] Jung Y, Bauer G, Nolta JA. Concise review: induced pluripotent stem cell-derived mesenchymal stem cells: progress toward safe clinical products. Stem Cell 2012;30:42–7. https://doi.org/10.1002/STEM.727.
[3] Shi Y, Inoue H, Wu JC, Yamanaka S. Induced pluripotent stem cell technology: a decade of progress. Nat Rev Drug Discov 2016 162 2016;16:115–30. https://doi.org/10.1038/nrd.2016.245.
[4] Girão AF, Semitela Â, Ramalho G, Completo A, Marques PAAP. Mimicking nature: fabrication of 3D anisotropic electrospun polycaprolactone scaffolds for cartilage tissue engineering applications. Compos B Eng 2018;154:99–107. https://doi.org/10.1016/j.compositesb.2018.08.001.
[5] Brito-Pereira R, Correia DM, Ribeiro C, Francesko A, Etxebarria I, Pérez-Álvarez L, et al. Silk fibroin-magnetic hybrid composite electrospun fibers for tissue engineering applications. Compos B Eng 2018;141:70–5. https://doi.org/10.1016/j.compositesb.2017.12.046.
[6] Lee JH, Lee JY, Yang SH, Lee EJ, Kim HW. Carbon nanotube-collagen three-dimensional culture of mesenchymal stem cells promotes expression of neural phenotypes and secretion of neurotrophic factors. Acta Biomater 2014;10:4425–36. https://doi.org/10.1016/j.actbio.2014.06.023.
[7] Gupta P, Agrawal A, Murali K, Varshney R, Beniwal S, Manhas S, et al. Differential neural cell adhesion and neurite outgrowth on carbon nanotube and graphene reinforced polymeric scaffolds. Mater Sci Eng C 2019;97:539–51. https://doi.org/10.1016/j.msec.2018.12.065.
[8] Shafiee A, Kehtari M, Zarei Z, Soleimani M, Varshochian R, Ahmadi A, et al. An in situ hydrogel-forming scaffold loaded by PLGA microspheres containing carbon nanotube as a suitable niche for neural differentiation. Mater Sci Eng C 2021;120:111739. https://doi.org/10.1016/j.msec.2020.111739.
[9] Shin J, Choi EJ, Cho JH, Cho AN, Jin Y, Yang K, et al. Three-dimensional electroconductive hyaluronic acid hydrogels incorporated with carbon nanotubes and polypyrrole by catechol-mediated dispersion enhance neurogenesis of human neural stem cells. Biomacromolecules 2017;18:3060–72. https://doi.org/10.1021/acs.biomac.7b00568.
[10] Lee SJ, Zhu W, Nowicki M, Lee G, Heo DN, Kim J, et al. 3D printing nano conductive multi-walled carbon nanotube scaffolds for nerve regeneration. J Neural Eng 2018;15. https://doi.org/10.1088/1741-2552/aa95a5.
[11] Kharaziha M, Shin SR, Nikkhah M, Topkaya SN, Masoumi N, Annabi N, et al. Tough and flexible CNT-polymeric hybrid scaffolds for engineering cardiac constructs. Biomaterials 2014;35:7346–54. https://doi.org/10.1016/j.biomaterials.2014.05.014.
[12] Ren J, Xu Q, Chen X, Li W, Guo K, Zhao Y, et al. Superaligned carbon nanotubes guide oriented cell growth and promote electrophysiological homogeneity for synthetic cardiac tissues. Adv Mater 2017;29:1702713. https://doi.org/10.1002/ADMA.201702713.
[13] Ahadian S, Yamada S, Ramón-Azcón J, Estili M, Liang X, Nakajima K, et al. Hybrid hydrogel-aligned carbon nanotube scaffolds to enhance cardiac differentiation of embryoid bodies. Acta Biomater 2016;31:134–43. https://doi.org/10.1016/j.actbio.2015.11.047.
[14] Shin SR, Shin C, Memic A, Shadmehr S, Miscuglio M, Jung HY, et al. Aligned carbon nanotube-based flexible gel substrates for engineering biohybrid tissue actuators. Adv Funct Mater 2015;25:4486–95. https://doi.org/10.1002/adfm.201501379.
[15] Lee J, Manoharan V, Cheung L, Lee S, Cha BH, Newman P, et al. Nanoparticle-based hybrid scaffolds for deciphering the role of multimodal cues in cardiac tissue engineering. ACS Nano 2019;13:12525–39. https://doi.org/10.1021/acsnano.9b03050.
[16] Dong R, Ma PX, Guo B. Conductive biomaterials for muscle tissue engineering. Biomaterials 2020;229. https://doi.org/10.1016/J.BIOMATERIALS.2019.119584.
[17] Shin SR, Bae H, Cha JM, Mun JY, Chen YC, Tekin H, et al. Carbon nanotube reinforced hybrid microgels as scaffold materials for cell encapsulation. ACS Nano 2012;6:362–72. https://doi.org/10.1021/nn203711s.
[18] Cellot G, Cilia E, Cipollone S, Rancic V, Sucapane A, Giordani S, et al. Carbon nanotubes might improve neuronal performance by favouring electrical shortcuts. Nat Nanotechnol 2009;4:126–33. https://doi.org/10.1038/NNANO.2008.374.
[19] Béduer A, Seichepine F, Flahaut E, Loubinoux I, Vaysse L, Vieu C. Elucidation of the role of carbon nanotube patterns on the development of cultured neuronal cells. Langmuir 2012;28:17363–71. https://doi.org/10.1021/LA304278N.
[20] Zhang X, Prasad S, Niyogi S, Morgan A, Ozkan M, Ozkan CS. Guided neurite growth on patterned carbon nanotubes. Sensor Actuator B Chem 2005;106:843–50. https://doi.org/10.1016/J.SNB.2004.10.039.
[21] Li Y, Huang G, Zhang X, Wang L, Du Y, Lu TJ, et al. Engineering cell alignment in vitro. Biotechnol Adv 2014;32:347–65. https://doi.org/10.1016/j.biotechadv.2013.11.007.
[22] Lorite GS, Ylä-Outinen L, Janssen L, Pitkänen O, Joki T, Koivisto JT, et al. Carbon nanotube micropillars trigger guided growth of complex human neural stem cells networks. Nano Res 2019;12:2894–9. https://doi.org/10.1007/s12274-019-2533-2.
[23] Xie XL, Mai YW, Zhou XP. Dispersion and alignment of carbon nanotubes in polymer matrix: a review. Mater Sci Eng R Rep 2005;49:89–112. https://doi.org/10.1016/J.MSER.2005.04.002.
[24] Cole MT, Cientanni V, Milne WI. Horizontal carbon nanotube alignment. Nanoscale 2016;8:15836. https://doi.org/10.1039/c6nr04666e.
[25] Goh GL, Agarwala S, Yeong WY. Directed and on-demand alignment of carbon nanotube: a review toward 3D printing of electronics. Adv Mater Interfac 2019;6. https://doi.org/10.1002/ADMI.201801318.
[26] Vader D, Kabla A, Weitz D, Mahadevan L. Strain-induced alignment in collagen gels. PLoS One 2009;4:e5902. https://doi.org/10.1371/JOURNAL.PONE.0005902.
[27] CM V, M K, RA M, JP S. Directional conductivity in SWNT-collagen-fibrin composite biomaterials through strain-induced matrix alignment. J Biomed Mater Res 2008;86:269–77. https://doi.org/10.1002/JBM.A.32029.
[28] Wang L, Wu Y, Guo B, Ma PX. Nanofiber yarn/hydrogel core-shell scaffolds mimicking native skeletal muscle tissue for guiding 3D myoblast alignment, elongation, and differentiation. ACS Nano 2015;9:9167–79. https://doi.org/10.1021/acsnano.5b03644.
[29] Koivisto JT, Joki T, Parraga JE, Paakkönen R, Yla-Outinen L, Salonen L, et al. Bioamine-crosslinked gellan gum hydrogel for neural tissue engineering. Biomed Mater 2017;12:025014. https://doi.org/10.1088/1748-605X/aa62b0.
[30] Kordás K, Mustonen T, Tóth G, Jantunen H, Lajunen M, Soldano C, et al. Inkjet printing of electrically conductive patterns of carbon nanotubes. Small 2006;2:1021–5. https://doi.org/10.1002/smll.200600061.
[31] Filippi M, Garello F, Yasa O, Kasamkattil J, Scherberich A, Katzschmann RK, et al. Engineered magnetic nanocomposites to modulate cellular function. Small 2021:2104079. https://doi.org/10.1002/SMLL.202104079.
[32] Ahadian S, Ramón-Azcón J, Estili M, Liang X, Ostrovidov S, Shiku H, et al. Hybrid hydrogels containing vertically aligned carbon nanotubes with anisotropic electrical conductivity for muscle myofiber fabrication. Sci Rep 2014;4:1–11. https://doi.org/10.1038/srep04271.
[33] Ramón-Azcón J, Ahadian S, Estili M, Liang X, Ostrovidov S, Kaji H, et al. Dielectrophoretically aligned carbon nanotubes to control electrical and mechanical properties of hydrogels to fabricate contractile muscle myofibers. Adv Mater 2013;25:4028–34. https://doi.org/10.1002/adma.201301300.
[34] Serrano MC, Gutiérrez MC, Del Monte F. Role of polymers in the design of 3D carbon nanotube-based scaffolds for biomedical applications. Prog Polym Sci 2014;39:1448–71. https://doi.org/10.1016/j.progpolymsci.2014.02.004.
[35] Stafford RJ. The physics of magnetic resonance imaging safety. Magn Reson Imag Clin N Am 2020;28:517–36. https://doi.org/10.1016/j.mric.2020.08.002.
[36] Reddy LH, Arias JL, Nicolas J, Couvreur P. Magnetic nanoparticles: design and characterization, toxicity and biocompatibility, pharmaceutical and biomedical applications. Chem Rev 2012;112:5818–78. https://doi.org/10.1021/cr300068p.
[37] Luo Z, Paunović N, Leroux JC. Physical methods for enhancing drug absorption from the gastrointestinal tract. Adv Drug Deliv Rev 2021;175. https://doi.org/10.1016/j.addr.2021.05.024.
[38] Administration USF and D. Criteria for significant risk investigations of magnetic resonance diagnostic devices-guidance for industry and food and drug administration staff. Silver Spring, MD US Food Drug Adm 2014:2014.
[39] Kordás K, Mustonen T, Toth G, Vähäkangas J, Uusimäki A, Jantunen H, et al. Magnetic-field induced efficient alignment of carbon nanotubes in aqueous solutions. Chem Mater 2007;19:787–91. https://doi.org/10.1021/cm062196t.
[40] Koivisto JT, Gering C, Karvinen J, Maria Cherian R, Belay B, Hyttinen J, et al. Mechanically biomimetic gelatin–gellan gum hydrogels for 3D culture of beating human cardiomyocytes. ACS Appl Mater Interfaces 2019;11:20589–602. https://doi.org/10.1021/acsami.8b22343.
[41] Gering C, Rasheed A, Koivisto JT, Párraga J, Tuukkanen S, Kellomäki M. Chemical modification strategies for viscosity-dependent processing of gellan gum. Carbohydr Polym 2021;269. https://doi.org/10.1016/J.CARBPOL.2021.118335.
[42] Gong Y, Wang C, Lai RC, Su K, Zhang F, Wang D-A. An improved injectable polysaccharide hydrogel: modified gellan gum for long-term cartilage regeneration in vitro n.d. https://doi.org/10.1039/b818090c.
[43] López-Cebral R, Paolicelli P, Romero-Caamaño V, Seijo B, Casadei MA, Sanchez A. Spermidine-cross-linked hydrogels as novel potential platforms for pharmaceutical applications. J Pharmacol Sci 2013;102:2632–43. https://doi.org/10.1002/jps.23631.
[44] Cao A, Veedu VP, Yao Z, Ghasemi-nejhad MN, Ajayan PM. Multifunctional brushes made from carbon nanotubes. 2005. https://doi.org/10.1038/nmat1415.
[45] Halonen N, Rautio A, Leino AR, KyllÖnen T, Tóth G, Lappalainen J, et al. Three-dimensional carbon nanotube scaffolds as particulate filters and catalyst support

membranes. ACS Nano 2010;4:2003. https://doi.org/10.1021/NN100150X/SUPPL_FILE/NN100150X_SI_001.PDF. –8.
[46] Toth G, Mäklin J, Halonen N, Palosaari J, Juuti J, Jantunen H, et al. Carbon-nanotube-based electrical brush contacts. Adv Mater 2009;21:2054. https://doi.org/10.1002/ADMA.200802200. –8.
[47] Gering C, Koivisto JT, Parraga JE, Kellomäki M. In: Eskola H, Väisänen O, Viik J, Hyttinen J, editors. Reproducible preparation method of hydrogels for cell culture applications – case study with spermidine crosslinked gellan gum BT - EMBEC & NBC 2017. Singapore: Springer Singapore; 2018. p. 811–4.
[48] Dewhurst Charles. Grasp _V9 2020. https://www.ill.eu/users/support-labs-infrastructure/software-scientific-tools/grasp.
[49] Gabriela Lorite, Janne Koivisto, Andrea Lassenberger, Anne Martel, Lionel Porcar. Structure of aligned carbon nanotubes/gellan gum hybrid hydrogels for guided neural cell growth. 2020. https://doi.org/10.5291/ILL-DATA.9-11-1960.
[50] Sasview 2018. http://www.sasview.org.
[51] Aktulga HM, Fogarty JC, Pandit SA, Grama AY. Parallel reactive molecular dynamics: numerical methods and algorithmic techniques. Parallel Comput 2012;38:245–59. https://doi.org/10.1016/J.PARCO.2011.08.005.
[52] Plimpton S. Fast parallel algorithms for short-range molecular dynamics. J Comput Phys 1995;117:1–19. https://doi.org/10.1006/JCPH.1995.1039.
[53] JJ S. Optimization of parameters for semiempirical methods VI: more modifications to the NDDO approximations and re-optimization of parameters. J Mol Model 2013;19:1–32. https://doi.org/10.1007/S00894-012-1667-X.
[54] Stewart JJP. Application of Localized Molecular Orbitals to the Solution of Semiempirical Self-Consistent Field Equations n.d. https://doi.org/10.1002/(SICI)1097-461X(1996)58:2.
[55] James SCC, Stewart SCC JP. MOPAC2016 program. 2016.
[56] Mäklin J, Halonen N, Toth G, Sápi A, Kukovecz Á, Kónya Z, et al. Thermal diffusivity of aligned multi-walled carbon nanotubes measured by the flash method. Phys Status Solidi B 2011;248:2508–11. https://doi.org/10.1002/pssb.201100143.
[57] Lipert K, Ritschel M, Leonhardt A, Krupskaya Y, Büchner B, Klingeler R. Magnetic properties of carbon nanotubes with and without catalyst. J Phys Conf 2010;200. https://doi.org/10.1088/1742-6596/200/7/072061.
[58] Chatterjee BK, Ghosh CK, Chattopadhyay KK. Temperature dependence of magnetization and anisotropy in uniaxial NiFe2O4 nanomagnets: deviation from the Callen-Callen power law. J Appl Phys 2014;116:153904. https://doi.org/10.1063/1.4898089.
[59] Mandal K, Mitra S, Kumar PA. Deviation from Bloch T3/2 law in ferrite nanoparticles. Europhys Lett 2006;75:618. https://doi.org/10.1209/EPL/I2006-10148-Y.
[60] Chang I, Im J, Lee SW, Cho GC. Strength durability of gellan gum biopolymer-treated Korean sand with cyclic wetting and drying. Construct Build Mater 2017;143:210–21. https://doi.org/10.1016/J.CONBUILDMAT.2017.02.061.
[61] Cassanelli M, Prosapio V, Norton I, Mills T. Acidified/basified gellan gum gels: the role of the structure in drying/rehydration mechanisms. Food Hydrocolloids 2018;82:346–54. https://doi.org/10.1016/J.FOODHYD.2018.04.024.
[62] Brown ZK, Fryer PJ, Norton IT, Bridson RH. Drying of agar gels using supercritical carbon dioxide. J Supercrit Fluids 2010;54:89–95. https://doi.org/10.1016/J.SUPFLU.2010.03.008.
[63] Cassanelli M, Prosapio V, Norton I, Mills T. Role of the drying technique on the low-acyl gellan gum gel structure: molecular and macroscopic investigations. 1947. https://doi.org/10.1007/s11947-018-2210-6.
[64] Vuornos K, Ojansivu M, Koivisto JT, Häkkänen H, Belay B, Montonen T, et al. Bioactive glass ions induce efficient osteogenic differentiation of human adipose stem cells encapsulated in gellan gum and collagen type I hydrogels. Mater Sci Eng C 2019;99:905–18. https://doi.org/10.1016/J.MSEC.2019.02.035.
[65] Gering C, Koivisto JT, Parraga J, Leppiniemi J, Vuornos K, Hytönen VP, et al. Design of modular gellan gum hydrogel functionalized with avidin and biotinylated adhesive ligands for cell culture applications. PLoS One 2019;14:e0221931. https://doi.org/10.1371/JOURNAL.PONE.0221931.
[66] Kavanagh GM, Ross-Murphy SB. Rheological characterisation of polymer gels. Prog Polym Sci 1998;23:533–62. https://doi.org/10.1016/S0079-6700(97)00047-6.
[67] Hyun K, Kim SH, Ahn KH, Lee SJ. Large amplitude oscillatory shear as a way to classify the complex fluids. J Non-Newtonian Fluid Mech 2002;107:51–65. https://doi.org/10.1016/S0377-0257(02)00141-6.
[68] Kocen R, Gasik M, Gantar A, Novak S. Viscoelastic behaviour of hydrogel-based composites for tissue engineering under mechanical load. Biomed Mater 2017;12:025004. https://doi.org/10.1088/1748-605X/aa5b00.
[69] Ahadian S, Ramón-Azcón J, Estili M, Liang X, Ostrovidov S, Shiku H, et al. Hybrid hydrogels containing vertically aligned carbon nanotubes with anisotropic electrical conductivity for muscle myofiber fabrication. Sci Rep 2015;4:4271. https://doi.org/10.1038/srep04271.
[70] Soares PAG, De Seixas Jrp C, Albuquerque PBS, Santos GRC, Mourão PAS, Barros W, et al. Development and characterization of a new hydrogel based on galactomannan and κ-carrageenan. Carbohydr Polym 2015;134:673–9. https://doi.org/10.1016/J.CARBPOL.2015.08.042.
[71] Yu MF, Lourie O, Dyer MJ, Moloni K, Kelly TF, Ruoff RS. Strength and breaking mechanism of multiwalled carbon nanotubes under tensile load. Science 2000;80(287):637–40. https://doi.org/10.1126/SCIENCE.287.5453.637.